Nanoscale

Accepted Manuscript

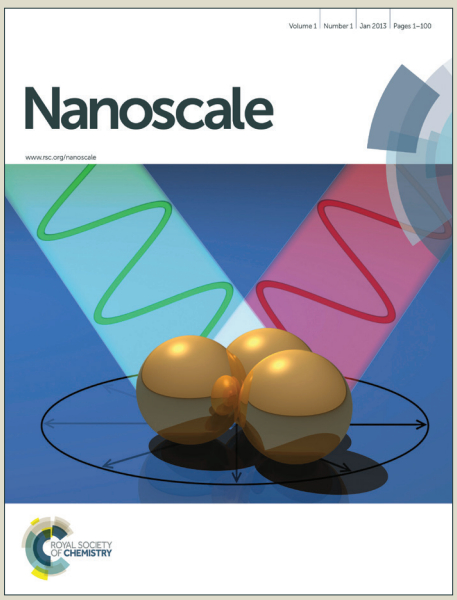

ROYAL SOCIETY OF CHEMISTRY

www.rsc.org/nanoscale

Nanoscale

RSCPublishing

COMMUNICATION

Selective Functionalization and Loading of Biomolecules in Crystalline Silicon Nanotube Field-Effect-Transistors

Soonshin Kwon, ‡[a], Zack C. Y. Chen, ‡[b], Hyunwoo Noh, ‡[a], Ju Hun Lee,[a] Hang Liu [a], Jennifer N. Cha,[c] and Jie Xiang*[ab]

Crystalline silicon nanotubes (Si-NTs) provide distinctive advantages as electrical and biochemical analysis scaffolds through their unique morphology and electrical tunability compared to solid nanowires or amorphous/non-conductive nanotubes. Such potentials are investigated in this report. Gate-dependent four probe current-voltage analysis reveals electrical properties such as resistivity to differ by nearly 3 orders between crystalline and amorphous Si-NTs. Analysis of transistor transfer characteristics yields field effect mobility of 40.0 $cm^2/V \cdot s$ in crystalline Si-NTs. The hollow morphology also allows selective inner/outer surface functionalization and loading capability either as a carrier for molecular targets or as nanofluidic channel for biomolecular assays. We present for the first time a demonstration of internalization of fluorescent dyes (Rhodamine) and biomolecules (BSA) in Si NTs as long as 22 μm in length.

In depth understanding of biomolecular interactions has led to more sophisticate diagnostics and therapeutic systems in the field of bioanalysis and biomedicine[1] and prompted the development of biosensors with ever improving specimen selectivity, signal-to-noise sensitivity, and variety of detectible biomaterials[2-5]. Silicon nanowires have shown their potential as an advanced biosensor platform[6-10] with real-time electrical readouts thanks to their reduced dimensionality, large surface-to-volume ratio, amplification of signal as an active field-effect device, selective surface modification for detecting specific targets, and abundant material processing knowledge derived from semiconductor manufacturing techniques.

Considerable efforts have been devoted to improve the performance of nanowire (NW) field-effect transistor (FET) biosensors. Point-like localized detection area along the NW axis via either dopant modulation[11] or p-n heterostructures[12] can enable finer spatial resolution and faster response. Multiplexing from nanowires array networks[13,14] have paved the way toward extreme sensitivity in the range of femtomolar precision since multiple sensor arrays on a single chip correlate effectively to discriminate electrical false-positive signals. Meanwhile, series of techniques involving modification of NW structure[15,16], device geometry[17] and functionalization of NW surfaces[18] have been demonstrated to further enhance the detection performance of NW FET biosensors. Beyond solid NWs, crystalline silicon nanotube[19] (c-Si NT) provides two distinctive inner and outer surfaces for analyte detection thus offering a new platform for novel applications as a biosenor. Unique morphology and non-cytotoxicity[20,21] of Si NTs endow them with potential functionality for intravascular drug delivery/imaging by using their inner cavity to load biomolecular species[21,22] Previously Shi et al. has examined the mechanism of one-dimensional nanostructure-cell interaction[23] while Ben-Ishai et al. has shown selective binding of metal nanoparticle either on inner or outer surfaces of Si NTs[24]. Meanwhile, electrically active high-quality c-Si NT themselves possess additional functionality as an FET channel sensitive to potential and charge modulations from environments both inside and outside. A combination of these traits makes c-Si NTs an attractive material for novel biosensor FET devices as recently demonstrated by Gao, R et al.[25].

In this report, we present a fundamental study of c-Si NT properties as a platform for electrically and biochemically functional devices. Synthesis of Si NTs shows well-controlled inner diameter (6~90 nm) and wall thickness (4~40 nm) by selectively etching core/shell Ge/Si nanowires (NWs). We used Ge/Si core/shell NWs as sacrificial templates to synthesize crystalline and amorphous Si NTs, as depicted in Figure 1a. Ge/Si core/shell NWs were grown using a two-step process[26,27]. The Si shell can be controlled to be epitaxially grown or amorphous by the process temperature. Following growth of core/shell NWs, Si NTs were synthesized by selective wet etching of Ge cores (see Supporting material for details). Figure 1b shows transmission electron microscope (TEM) image of as-synthesized c-Si NTs with inner diameter (ID) of 88±16 nm and 10 nm shell thickness. The ID is solely determined by the Ge core diameter during synthesis based on choice of the Au catalyst diameters. Using this method, NT with ID from 50 nm (figure 1c) and, by using 5 nm diameter catalysts, to as small as 6.5 nm surrounded by 4 nm thick Si shell can be synthesized (inset to Figure 1c). The NT shells have relatively uniform thickness with 1~2 nm fluctuations. High-resolution TEM (figure 1d) and fast Fourier transform (FFT) images (inset of Figure 1d) further reveal the highly crystalline nature of the c-Si NTs. The FFT shows the NT's <112> growth orientation with the measured 0.11 nm interatomic distance matching that of Si {224} planes[28]. The 6 sharp diffraction spots around the centre indicate

epitaxial deposition of Si layer following the Ge core. As shown in figure 1e, we found these crystalline NTs to preserve their crystallinity even after been exposed in air at room temperature for 28 days. There is also little discernable change in their oxide layer thickness (shown as the light contrast layers on the outer surface of the TEM images)[29]. Such stability is ideal for nanoelectronic and biomedical applications.

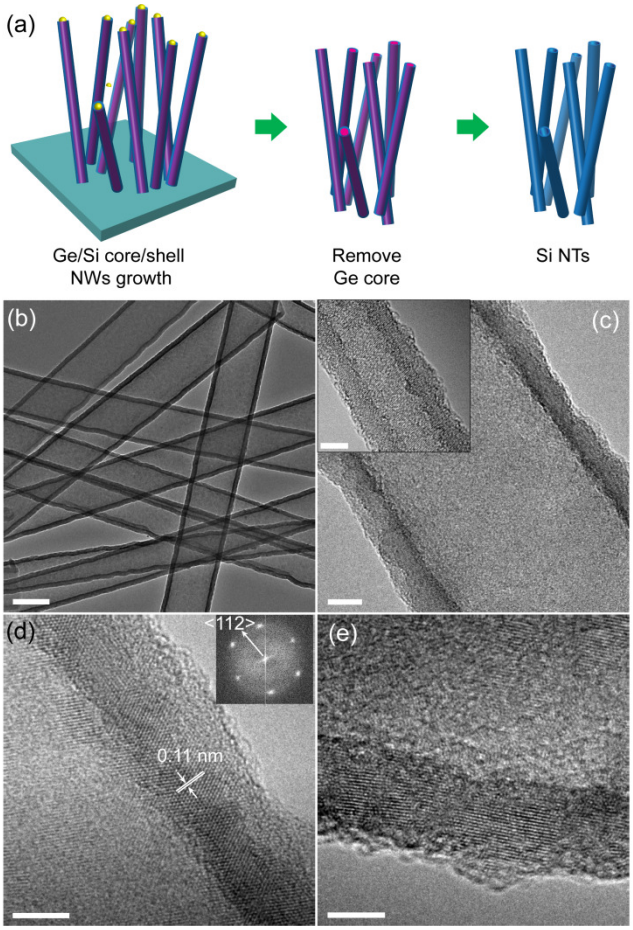

Figure 1. (a) Schematics of Si NT synthesis steps showing transformation from Ge/Si core/shell NWs to Si NT structures by etching away the Ge core. (b) Bundle of Si NTs shown in low-resolution TEM image and (c) Higher resolution image of individual NT with 50 nm ID and 9 nm shell thickness. Inset shows a NT with 6.5 nm ID with 4 nm shell. (d) High-resolution TEM shows the crystal lattice on the shell of representative Si NT. Fast Fourier transform (FFT) images in the inset indicates a <112> growth direction. (e) TEM from crystalline Si NT after 28 days exposed in air and its FFT pattern on the inset. Scale bars: 100 nm for panel (b) and 5 nm for (c), (d), and (e).

To establish the fundamental electrical properties of c-Si NTs, we performed four point probe measurement on c-Si FETs with 100 nm thick thermal oxide layer as the back-gate dielectrics (Figure 2a). The devices were fabricated using standard e-beam lithography, metallization, and lift-off techniques. Four metal contacts of 1 μm width were deposited on each NT FET with 150/30 nm thick Ni/Au bilayer followed by rapid thermal annealing at 400°C for 30 seconds to improve electrical contacts between Si and Ni. Four-probe measurements were carried out using HP 4155A semiconductor parameter analyser and SR560 voltage pre-amplifier to monitor the inner voltage drop V_{D23} while capturing I_D-V_{D14}. First, gated two-probe I-V measurement across electrodes 1 and 4 (top inset, figure 2b) shows typical p-type FET behaviour, where the drain current increases with more negative gate voltages and begins to saturate at negative bias voltage. Meanwhile the four probe I_D-V_{D23} measurement result (figure 2b) shows clear linear *I-V* curves indicating contact barriers are effectively eliminated. At V_G = -20 V, the two-probe resistance of the NT is 180 MΩ while only 4.4 MΩ when measured using the four-probe method, suggesting an average contact resistance of 88 MΩ which dominates the two-probe measurement results. Therefore, four-probe current-voltage (*I-V*) measurements are necessary in order to eliminate the effects from Schottky contact barriers at the Ni-Si contact interfaces and to represent intrinsic *I-V* characteristics of the NT material.

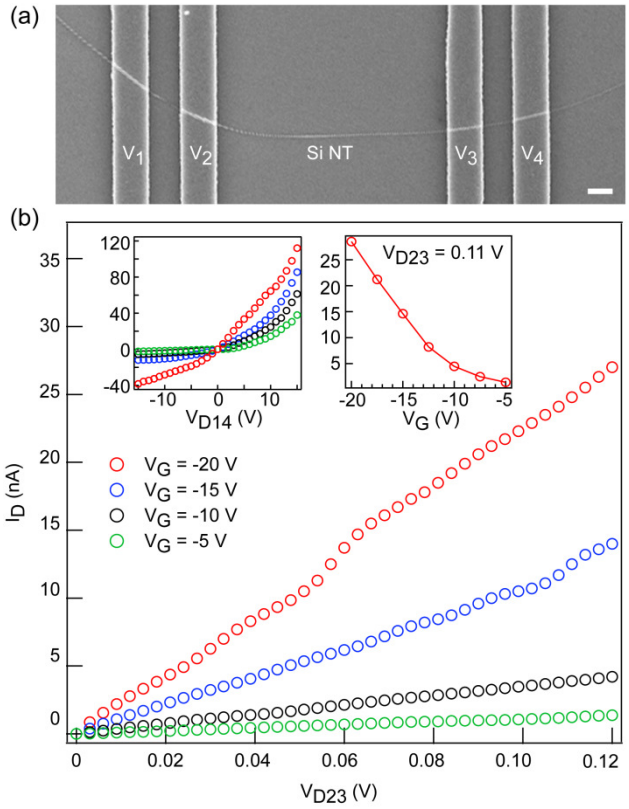

Figure 2. (a) Device SEM picture and (b) I_D-V characteristics under four different sets of gate biases from a representative c-Si NT FET with ID of 30 nm, shell thickness of 5 nm and length of 7.3 μm between the two inner contacts. The voltages on the four electrodes are indicated in the device SEM. Top left inset: two-probe *I-*V_{D23} characteristics across the two outer contacts. Top right inset: four-probe current versus gate bias V_G measured at an inner probe voltage of V_{D23} = 0.11 V. Scale bar in (a): 1 μm.

From the dimension of the NT and slopes of the linear I_D-V_{D23}, we can obtain the resistivity of crystalline Si NT to be 0.032, 0.069, 0.22, and 0.68 Ω·cm from gate voltage of -20 (red) to -5 V (green) with 5 V steps.

With decreasing gate bias, the four-probe NT conductance rises, representative of the linear-region transfer characteristics of a p-type FET[30] (top right inset, figure 2b), with transconductance (g_m = d*I*/dV_G) of 2.78 nS at V_{D23} = 0.11 V and an extrapolated threshold voltage of V_T = -9.9 V. From these values we can extract the low-field mobility μ based on a long channel transistor model using $\mu = g_m L^2/C_G V_{DS}$. For estimation of the gate capacitance C_G we used finite-element modelling similar to a previous study on the dielectric screening effect from low carrier density Si NWs[31] and found that back gate capacitance coupling to NTs is near identical to NWs across a wide range of carrier concentrations (see Supporting material). Field-effect mobility for the c-Si NT in Fig. 2 is 40.0

$cm^2/V \cdot s$, which is comparable to values reported in bulk polycrystalline Si with large grain sizes[32-34]. One can also obtain mobility from the Ohm's law using the Drude model: $\sigma = ne\mu = (V_G - V_T)C_G\mu/L^2$ which yields μ = 40.6 $cm^2/V \cdot s$. These robust performances attest to the highly crystalline nature of the electronically active Si nanotube channels.

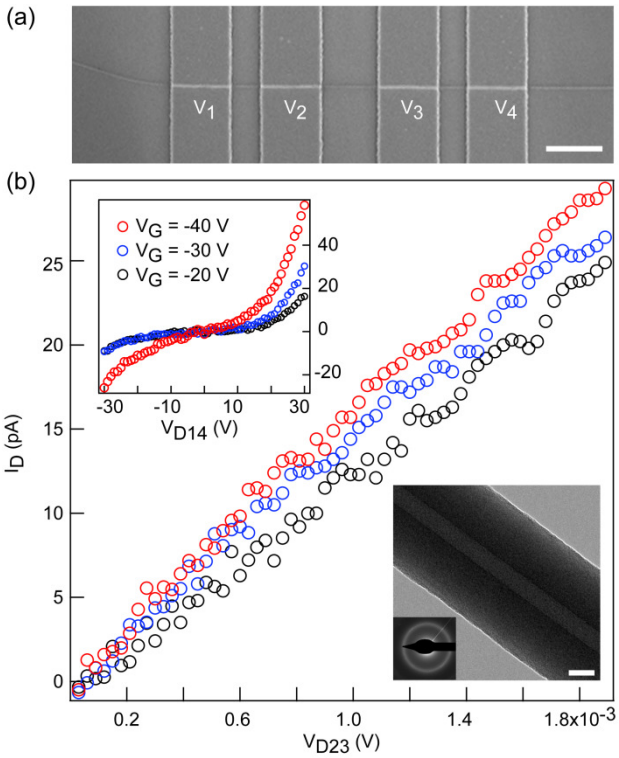

Figure 3. (a) Device SEM picture and (b) *I-V* characteristics under four different sets of gate biases from a representative a-Si NT FET with ID of 20 nm, shell thickness 40 nm and length of 2 μm between the two inner contacts. Top inset depicts corresponding two-probe *I-V* measurement and bottom inset shows TEM image of 40 nm thick amorphous Si NT with 20 nm core along with its SAED pattern in the inset. Scale bar, (a) 2 μm and bottom inset of (b) 20 nm.

The high conductivity of our c-Si NTs is also evident when compared with *I-V* measurement of amorphous Si NT (a-Si NT) FETs. We intentionally synthesized a-Si NTs using a modified growth recipe with Si shell growth at a lower temperature (see Supporting materials) for 2 hrs which produced 40 nm thick amorphous shells as confirmed by TEM and the lack of distinctive spots from selected area electron diffraction (SAED) patterns (figure 3b). Compared to the thin, 4~5 nm thick c-Si NTs, here a thick a-Si shell thickness was necessary to achieve measureable conductance above the noise level of our measurement system. a-Si NTFET device was fabricated with four 2 μm wide Ni/Au contacts and an inner channel length of 2 μm (Figure 3a). Two probe I_D-V_{D14} measurement (top inset of Figure 3) shows non-linear, Schottky contact behaviour and p-type characteristics with a maximum on current of less than 50 pA under 30 V bias with V_G as small as -40 V. Four-probe conductance in Figure 3b shows an intrinsic resistivity of 28.8, 24.8, and 22.7 Ω·cm for -20, -30, and -40 V gate bias respectively with more apparent noise in the *I-V* curves due to the low current level. These values in a-Si NT are nearly 3 orders more resistive than the on-state resistivity from c-Si NTs. Such difference is a direct result of their respective morphologies.

Previously extensively studies have shown decoration of Si NWs with a wide selection of biomolecules with help from covalently bonded silane chemistry[6,35]. To explore the potential integration and compatibility of our c-Si NTs with bio-specimens, in particular the capability of introducing analytes on the inner surface and cavity of the NT, we have further studied selective surface functionalization on the NT's inner and outer surfaces (Figure 4). The outer silicon surface was first selectively functionalized with polyethylene glycol (PEGylation) as a stealth moiety. We begin with outer surface PEGylation of the as-grown core/shell NWs using trimethoxysilane PEG (2 kDa, ProChimia) upon immediate cool-down and removal from the growth chamber (see Supporting materials). PEGylated NWs are cleaved and suspended in solvent using an ultrasonicator to expose the fresh Ge on the ends. This is followed by etch removal of the Ge core to form hollow SiNTs with the inner surface being fresh Si while outer surface protected by PEG (Fig. 4a).

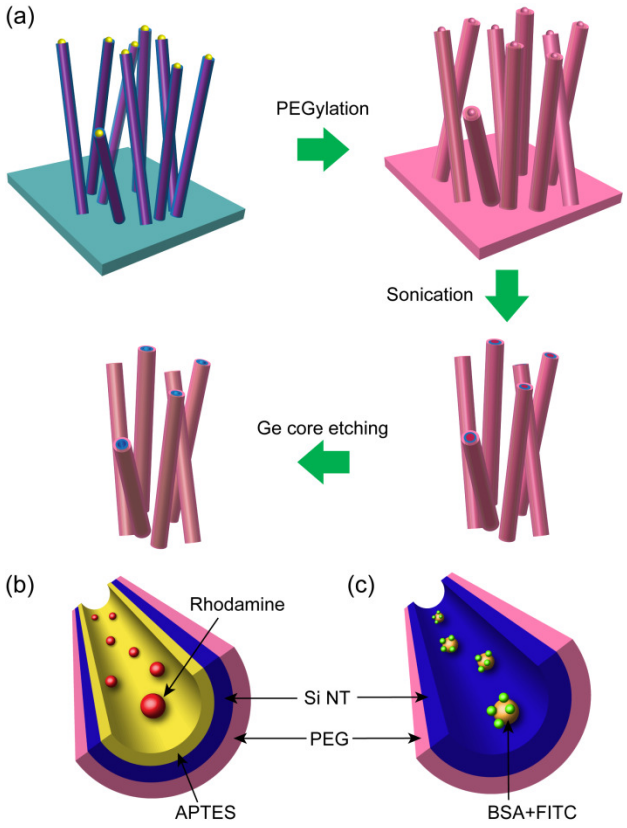

Figure 4. Schematic illustration of selective biomolecule functionalization. (a) PEGylation process on the outer wall of Si NTs followed by Ge core removal for inner wall functionalization. (b) Two types of biomolecules, Rhodamine and BSA-FITC, loading inside the cavity of Si NTs.

Here we demonstrate loading of two different molecules, Rhodamine (Figure 4b) and bovine serum albumin (BSA)-fluorescein isothiocyanate (FITC) conjugates (Figure 4c) into Si NTs. The Rhodamine and FITC are red and green fluorescent respectively and are used to help visualize the loading results. The average ID size of NTs used is 30 nm.

First, for loading of Rhodamine molecules, 3-aminopropyltriethoxysilane (APTES) was used as a self-assembled monolayer on the inner surface of the SiNT to enable covalent bonding to the carboxylic group on Rhodamine (see Supporting materials for details). Far-field fluorescent optical images (Figure 5a

and b right panels) along with corresponding bright-field images (Figure 5a and b left panels) of functionalized Si NTs show a fluorescent rod-shaped structure 5 μm in length suggesting the successful functionalization of Rhodamine in the Si NTs. As a control experiment and to verify that Rhodamine is not attached to the outer surfaces, we performed the same functionalization procedures on solid core Ge/Si core/shell NWs. The solid NW surfaces are identical to the outer surface of hollow NTs and are PEGlyated via the same procedure. Absence of fluorescence (Figure 5c right panel) compared to the NW in the corresponding bright-field image (Figure 5c left panel) confirms the high selectivity of functionalization on the nanotube inner surface only and demonstrates the high quality PEGylation on the outer Si surface preventing any side reaction with APTES or fluorescent molecules which could be attached directly onto Si. Therefore we have shown that with protective PEGylation of the outer surface, the inner surface of the Si NT can be selectively functionalized and loaded with small molecules.

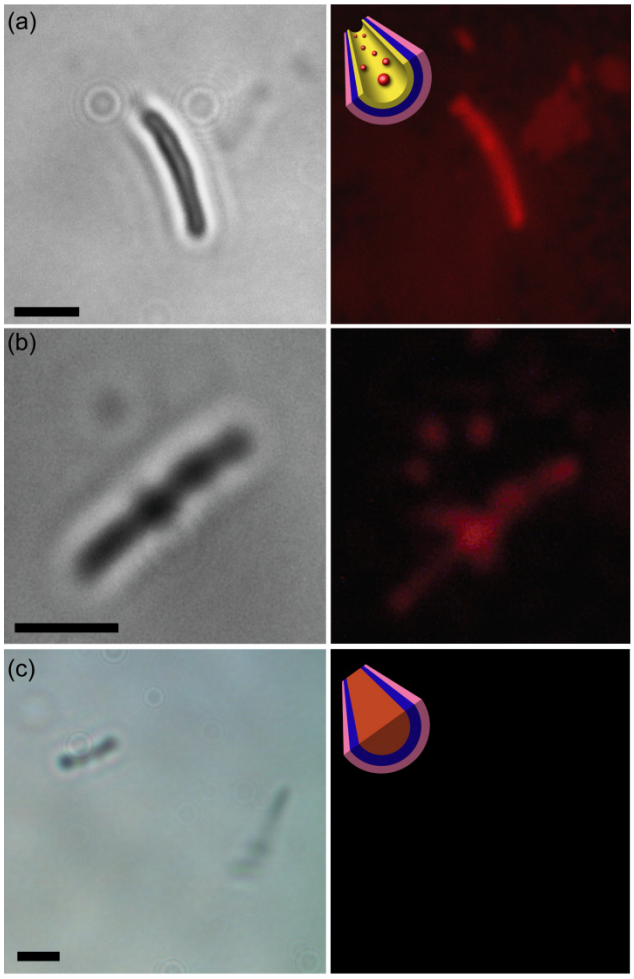

Figure 5. Demonstration of Rhodamine loading. (a) and (b) Bright field (left) and fluorescent (right) images showing red fluorescent signals in Rhodamine-loaded Si NTs. (c) Control sample after APTES functionalization and incubation with Rhodamine using a solid core Ge/Si nanowire, showing no fluorescent signals. Scale bars, 3 μm.

Beyond fluorescent dyes, we further experimented with a larger, FITC decorated BSA molecule loaded inside Si NTs (Figure 6). BSA is a single polypeptide chain with 580 amino acid residues, and contains 17 intrachain dissulfie bridges and 1 sulfhydryl group[36]. A BSA protein is approximately 14 nm x 4 nm x 4 nm in size. From the right panel of figure 6a, rod-shaped green fluorescence signals are clearly observed in NTs shown in the bright field image (figure 6a, left), indicating fluorescently functionalized proteins (BSA) are successfully loaded within Si NTs. Significantly, figure 6a shows loading of BSA in an NT as long as 22 μm. Similar to the case with Rhodamine, a control experiment loading BSA-FITC into solid core/shell Ge/Si NWs shows no fluorescence from its outer surface (figure 6b, right) of the corresponding NWs in the bright-field image (figure 6b, left), which again demonstrates the lack of leakage path or side reaction through the encapsulated PEG layers on the outer surface of Si NTs or NWs and most importantly, the successful selective functionalization of the inner walls of Si NTs by relatively large protein molecules.

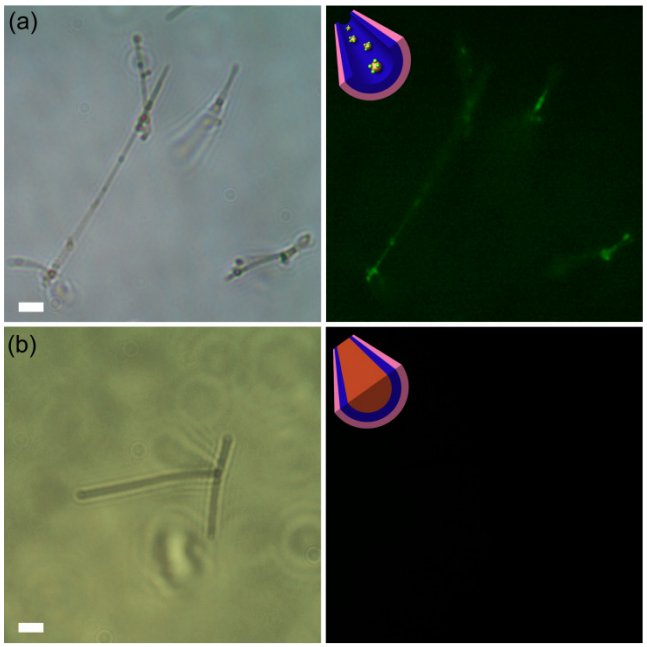

Figure 6. Demonstration of BSA-FITC functionalization. (a) BSA-FITC-loaded Si NTs from bright field (left) shows green fluorescent (right) signals while (b) control sample of a solid Ge/Si nanowire functionalized in the same condition presents no fluorescent signal. Scale bars, 5 μm

In summary, we have explored the potential of crystalline Si NTs as an electrically active and biochemically compatible material in ways that distinguish them from solid NWs. TEM analysis reveals the crystalline nature of the as-synthesized NTs. Four probe transport analysis yields field effect mobility of 40 $cm^2/V \cdot sec$ for the c-Si NT and a resistivity as small as 0.032 $\Omega \cdot cm$, nearly 3 orders more conductive than that of amorphous Si NTs. Such demonstrated electrical property in c-Si NTs may extend to much broader applications such as high efficiency thermoelectric modules due to phonon confinement effects in Si NTs[37,38]. Moreover, by selectively functionalizing the inner/outer surfaces, we demonstrated uptake of molecules from small dye molecules to proteins bonded on the NT inner surface, which when combined with the electrically active NT channel have the potential to lead to a range of novel therapeutic drug delivery or diagnostic detection applications[39-41].

Acknowledgement

We acknowledge the use of the UCSD Cryo-Electron Microscopy Facility which is supported by NIH grants to Dr. Timothy S. Baker and a gift from the Agouron Institute to UCSD. Z.C. acknowledges the help from Dr. Sadik C. Esener and Dr. Andrew P. Goodwin with the fluorescent microscope measurements. This work is supported by the NSF Award ECCS-0955199 and CBET-1336428. J.X. acknowledges support from the Hellman Fellowship.

Notes and references

[a] Materials Science and Engineering Program, University of California, San Diego, La Jolla, California 92093, United States.
[b] Department of Electrical and Computer Engineering, University of California, San Diego, La Jolla, California 92093, United States.
[c] Department of Chemical and Biological Engineering, University of Colorado, Boulder

† Electronic Supplementary Information (ESI) available: modelling (Fig.S1) and experimental details.

‡ These authors contributed equally to this work.

1. T. A. Manolio, F. S. Collins, N. J. Cox, D. B. Goldstein, L. A. Hindorff, D. J. Hunter, M. I. McCarthy, E. M. Ramos, L. R. Cardon, A. Chakravarti, J. H. Cho, A. E. Guttmacher, A. Kong, L. Kruglyak, E. Mardis, C. N. Rotimi, M. Slatkin, D. Valle, A. S. Whittemore, M. Boehnke, A. G. Clark, E. E. Eichler, G. Gibson, J. L. Haines, T. F. C. Mackay, S. A. McCarroll and P. M. Visscher, *Nature*, 2009, **461**, 747.
2. S. Sorgenfrei, C.-y. Chiu, R. L. Gonzalez, Y.-J. Yu, P. Kim, C. Nuckolls and K. L. Shepard, *Nat. Nano.*, 2011, **6**, 126.
3. A. J. Haes and R. P. Van Duyne, *J. Am. Chem. Soc.*, 2002, **124**, 10596.
4. B. A. Cornell, V. Braach-Maksvytis, L. King, P. Osman, B. Raguse, L. Wieczorek and R. Pace, *Nature*, 1997, **387**, 580.
5. X. Duan, T.-M. Fu, J. Liu and C. M. Lieber, *Nano Today*, 2013, **8**, 351.
6. Y. Cui, Q. Wei, H. Park and C. M. Lieber, *Science*, 2001, **293**, 1289.
7. F. Patolsky, B. P. Timko, G. Yu, Y. Fang, A. B. Greytak, G. Zheng and C. M. Lieber, *Science*, 2006, **313**, 1100.
8. T. Cohen-Karni, B. P. Timko, L. E. Weiss and C. M. Lieber, *Proc. Natl. Acad. Sci. U.S.A.*, 2009, **106**, 7309.
9. M. M. A. Hakim, M. Lombardini, K. Sun, F. Giustiniano, P. L. Roach, D. E. Davies, P. H. Howarth, M. R. R. de Planque, H. Morgan and P. Ashburn, *Nano Lett.*, 2012, **12**, 1868.
10. K.-I. Chen, B.-R. Li and Y.-T. Chen, *Nano Today*, 2011, **6**, 131.
11. T. Cohen-Karni, D. Casanova, J. F. Cahoon, Q. Qing, D. C. Bell and C. M. Lieber, *Nano Lett.*, 2012, **12**, 2639.
12. Z. Jiang, Q. Qing, P. Xie, R. Gao and C. M. Lieber, *Nano Lett.*, 2012, **12**, 1711.
13. G. Zheng, F. Patolsky, Y. Cui, W. U. Wang and C. M. Lieber, *Nat Biotech*, 2005, **23**, 1294.
14. B. P. Timko, T. Cohen-Karni, G. Yu, Q. Qing, B. Tian and C. M. Lieber, *Nano Lett.*, 2009, **9**, 914.
15. B. Tian, T. Cohen-Karni, Q. Qing, X. Duan, P. Xie and C. M. Lieber, *Science*, 2010, **329**, 830.
16. X. Duan, R. Gao, P. Xie, T. Cohen-Karni, Q. Qing, H. S. Choe, B. Tian, X. Jiang and C. M. Lieber, *Nat.Nanotechnol.*, 2011, **7**, 174.
17. J.-H. Ahn, S.-J. Choi, J.-W. Han, T. J. Park, S. Y. Lee and Y.-K. Choi, *Nano Lett.*, 2010, **10**, 2934.
18. A. Gao, N. Zou, P. Dai, N. Lu, T. Li, Y. Wang, J. Zhao and H. Mao, *Nano Lett.*, 2013, **13**, 4123.
19. M. B. Ishai and F. Patolsky, *J. Am. Chem. Soc.*, 2009, **131**, 3679.
20. D. K. Nagesha, M. A. Whitehead and J. L. Coffer, *Adv. Mater.*, 2005, **17**, 921.
21. A. Nan, X. Bai, S. J. Son, S. B. Lee and H. Ghandehari, *Nano Lett.*, 2008, **8**, 2150.
22. Z. Liu, X. Sun, N. Nakayama-Ratchford and H. Dai, *ACS Nano*, 2007, **1**, 50.
23. X. Shi, A. von dem Bussche, R. H. Hurt, A. B. Kane and H. Gao, *Nat. Nano.*, 2011, **6**, 714.
24. M. Ben-Ishai and F. Patolsky, *J. Am. Chem. Soc.*, 2011, **133**, 1545.
25. R. Gao, S. Strehle, B. Tian, T. Cohen-Karni, P. Xie, X. Duan, Q. Qing and C. M. Lieber, *Nano Lett.*, 2012, **12**, 3329.
26. V. Schmidt, J. V. Wittemann, S. Senz and U. Gösele, *Adv. Mater.*, 2009, **21**, 2681.
27. Y. Wu, Y. Cui, L. Huynh, C. J. Barrelet, D. C. Bell and C. M. Lieber, *Nano Lett.*, 2004, **4**, 433.
28. H. Y-J, L. Alois, S. Mathias, B. Emmerich and P. Peter, *Nanotechnology*, 2009, **20**, 125606.
29. H. Cui, C. X. Wang and G. W. Yang, *Nano Lett.*, 2008, **8**, 2731.
30. M. Mongillo, P. Spathis, G. Katsaros, P. Gentile and S. De Franceschi, *Nano Lett.*, 2012, **12**, 3074.
31. D. Khanal and J. Wu, *Nano Lett.*, 2007, **7**, 2778.
32. M. K. Hatalis and D. W. Greve, *Electron Device Lett.*, 1987, **8**, 361.
33. Z. Wei, M. Zhiguo, Z. Shuyun, Z. Meng, C. Rongsheng, W. Man and K. Hoi-Sing, *Electron Device Lett.*, 2012, **33**, 1414.
34. M. Zhiguo, Z. Shuyun, W. Chunya, Z. Bo, W. Man and K. Hoi-Sing, *J. Display Technol.*, 2006, **2**, 265.
35. F. Patolsky, G. Zheng and C. M. Lieber, *Anal. Chem.*, 2006, **78**, 4260.
36. Y. L. Jeyachandran, E. Mielczarski, B. Rai and J. A. Mielczarski, *Langmuir*, 2009, **25**, 11614.
37. J. Chen, G. Zhang and B. Li, *Nano Lett.*, 2010, **10**, 3978.
38. S. Kwon, Z. C. Chen, J.-H. Kim and J. Xiang, *Nano Lett.*, 2012, **12**, 4757.
39. A. S. Determan, B. G. Trewyn, V. S. Y. Lin, M. Nilsen-Hamilton and B. Narasimhan, *J. Controlled Release*, 2004, **100**, 97.
40. T. L. Krause and G. D. Bittner, *Proc. Natl. Acad. Sci. U.S.A.*, 1990, **87**, 1471.
41. K. S. Russell, M. P. Haynes, D. Sinha, E. Clerisme and J. R. Bender, *Proc. Natl. Acad. Sci. U.S.A.*, 2000, **97**, 5930.